On the Impact of Turbulent Inflow on the Noise Generated by a Propeller Operating at Low Reynolds Number

Original
On the Impact of Turbulent Inflow on the Noise Generated by a Propeller Operating at Low Reynolds Number / Ali, Mario; Piccolo, Andrea; Zamponi, Riccardo; Ragni, Daniele; Avallone, Francesco. - (2025), pp. 1737-1744. (Forum Acusticum Euronoise 2025. 11th Convention of the European Acoustics Association Malaga (ESP) 23-26 June 2025) [10.61782/fa.2025.0647].

Publisher:
European Acoustics Association, EAA

Published
DOI:10.61782/fa.2025.0647

DOI: 10.61782/fa.2025.0647

FORUM ACUSTICUM
EURONOISE 2025

ON THE IMPACT OF TURBULENT INFLOW ON THE NOISE GENERATED BY A PROPELLER OPERATING AT LOW REYNOLDS NUMBER

Mario Alì[1*] **Andrea Piccolo**[2] **Riccardo Zamponi**[2,3]
Daniele Ragni[2] **Francesco Avallone**[1]
[1] Dipartimento di Ingegneria Meccanica e Aerospaziale, Politecnico di Torino, Torino, Italy
[2] Department of Flow Physics and Technology, Delft University of Technology, Delft, The Nederlands
[3] von Kàrmàn Institute for Fluid Dynamics, Rhode-Saint-Genèse, Belgium

ABSTRACT

Ingested turbulence affects propeller noise at frequencies higher than the 2nd blade passing frequency. The extension of Amiet's model to rotating blades represents a useful tool for predicting this phenomenon. However, it relies on assumptions that are not fully valid in reality, e.g., it neglects the distortion of turbulence. This paper investigates how the propeller-induced flow field alters incoming turbulence paving the way, in future studies, to extend Amiet's model with these features. Lattice Boltzmann Very Large Eddy Simulations of a reference propeller, for which experimental data exist, operating at low-Reynolds number and subject to turbulent inflow are performed. The spatial and temporal evolution of isotropic grid-generated turbulence approaching the propeller plane is characterized. It is found that the propeller leading edge interacts with anisotropic turbulence. This is due to the rotational flow induced by the propeller, stream tube contraction, and leading-edge distortion. In addition, the impact of the inflow turbulence on the laminar separation bubble on the propeller suction side, whose dynamic affects the acoustics at high frequencies, is analyzed. Finally, the aerodynamics flow features are linked to the far-field acoustic spectra, obtained through the Ffowcs-Williams and Hawkings analogy applied to the propeller surface.

Keywords: *turbulence ingestion noise, turbulence distortion, laminar separation bubble*

1. INTRODUCTION

The growing interest in small Unmanned Aerial Vehicles (UAVs), driven by a wide range of potential applications, poses the need to integrate this technology into an urban environment. Given their impact on public acceptance [1], it is crucial to account for the aerodynamic noise generated by these devices when operating in an urban environment, which is characterized by different scales of turbulence.

From an aerodynamic point of view, small UAVs' propellers typically operate at low Reynolds numbers, resulting in a transitional regime extremely susceptible to inflow disturbances and characterized by complex phenomena such as the presence of laminar separation bubble (LSB) [2]. Furthermore, incoming turbulence interacting with the propeller produces an unsteady pressure field over the surface, that is radiated as broadband and/or quasi-tonal noise in the far field [3, 4]. LSB, whose presence on a small propeller was assessed for the first time by Grande et al. [5] under clean inflow, plays an important role in the far-field noise in the high-frequency [6]. It causes laminar boundary layer vortex shedding noise with frequency varying along the propeller radius, thus resulting in a high-frequency hump. Casalino et al. [2, 3] showed that, under clean inflow conditions, the mean behavior of the LSB is mostly determined by the propeller advance ratio; furthermore, in hovering, the mean LSB is

---

**Corresponding author*: *mario.ali@polito.it.*

unaffected by the recirculating flow in the testing environment.

Most of the work on rotors in turbulent inflow focuses on helicopter and engine rotors, typically operating at higher Reynolds numbers, and they do not consider the effect of turbulence on LSB. Sevik [7] proposed a prediction method of turbulence ingestion noise based on the two-dimensional aerodynamic response function and dipolar radiation pattern of the unsteady loading. This retrieved the broadband component of the acoustic spectrum but missed the quasi-tonal content. Blake [8] recovered the latter by introducing blade-to-blade correlation. Hanson [9] attributed the quasi-tonal noise to the streamwise elongation of the eddies that, chopped several times by the rotor, produce blade-to-blade coherence in the unsteady loading. This is reflected in the narrow-band content around the BPF harmonics in the acoustic spectrum.

Amiet extended the prediction model for airfoils in turbulent inflow [10] to the case of rotating blades [11] approximating the circular motion to a rectilinear motion in the limit of acoustic frequencies much higher than the rotational one. The model obtains the acoustic spectrum from the characteristics of incoming turbulence through an acoustic transfer function, neglecting the effects of turbulence distortion. Capobianchi et al. [12] employed two analytical models based on Amiet's theory for noise prediction: the first one considers turbulence characteristics at a specific representative radial location while the second accounts for blade geometry and turbulence parameters along the blade and exploits the inverse strip theory [13], providing better results. Raposo et al. [14] proposed a prediction model that includes the effects of rotation and spanwise coherence. They proved that Amiet's model recovers the haystacking tones when revised with a correct calculation of the time between two consecutive chops of the same eddy. They highlighted that haystacking is underpredicted when the integral length scale of the flow is large compared to the blade, likely because of the lack of spanwise correlation in the direct strip approach adopted. In these studies, the effect of including turbulence distortion in Amiet 's model is not considered.

The purpose of this study is two-fold. First, the analysis of turbulence near the leading edge reveals the effect of the propeller-induced flow field on the turbulent inflow, inspecting the validity of the assumptions of Amiet 's model. The effect of including turbulence distortion in Amiet 's model prediction will be presented in future work. Additionally, the solid formulation of the FWH analogy, applied to the propeller surface, allows to characterize the effects of ingested turbulence on the aerodynamic sources across different frequency ranges. To address these points, three different setups (only turbulence, propeller in turbulent inflow, and propeller in clean inflow) have been simulated in PowerFLOW 6-2022-R1 3DS.

The paper is structured as follows: the numerical setup is described in sec.2.2 and validated in sec.2.3. In sec.3 the main results are discussed, and sec.4 summarizes the conclusions of this work.

2. METHODOLOGY

2.1 Computational method

The study is based on data obtained with PowerFLOW 6-2022-R1, based on a Lattice-Boltzmann Method (LBM). Here, the only unknown quantity is the particle-probability distribution function $f(\mathbf{x}, t, \mathbf{v})$, representing the probability for a particle at location $\mathbf{x}$ and instant t to have velocity $\mathbf{v}$. The macroscopic quantities are retrieved from the statistical moments of f. The evolution of $f(\mathbf{x}, t, \mathbf{v})$ is described by the Boltzmann equation, which relies on gas-kinetic theory. The discrete Boltzmann equation is then solved on a Cartesian mesh, whose base elements are called voxels, whose size halves from a resolution region to the next finer one. Since reaching a y^+ lower than 1 in a Cartesian mesh is computationally prohibitive, a fully turbulent wall function model, extended to include the effects of pressure gradient, is adopted in this work.

2.2 Numerical setup

The computational domain is a cube with a side length of 100 D_{prop}. The region of interest with the turbulence grid and the propeller is located at the center of the computational domain, which is discretized into 17 Variable Resolution (VR) regions, numbered from 0 to 16, gradually increasing the resolution from the outer region to the area of interest. VR11 resolves the turbulence from the grid to $2D_{prop}$ downstream of the propeller plane, to enclose the nacelle. The voxel size in this region is 0.88 mm. 5 inner levels, defined as offsets of the blades, are introduced to achieve a $y^+_{MAX} \approx 9$ at the wall to capture the separation bubble [2, 3]. The total number of voxels in the computational domain is approximately 1.2×10^7, with the smallest voxel size equal to 0.03 mm. The numerical setup (fig.1) reproduces the experimental one [12]. The flow exits from a cylindrical pipe with a diameter $D = 0.6m$, whose wall is treated as frictionless. The turbulence grid

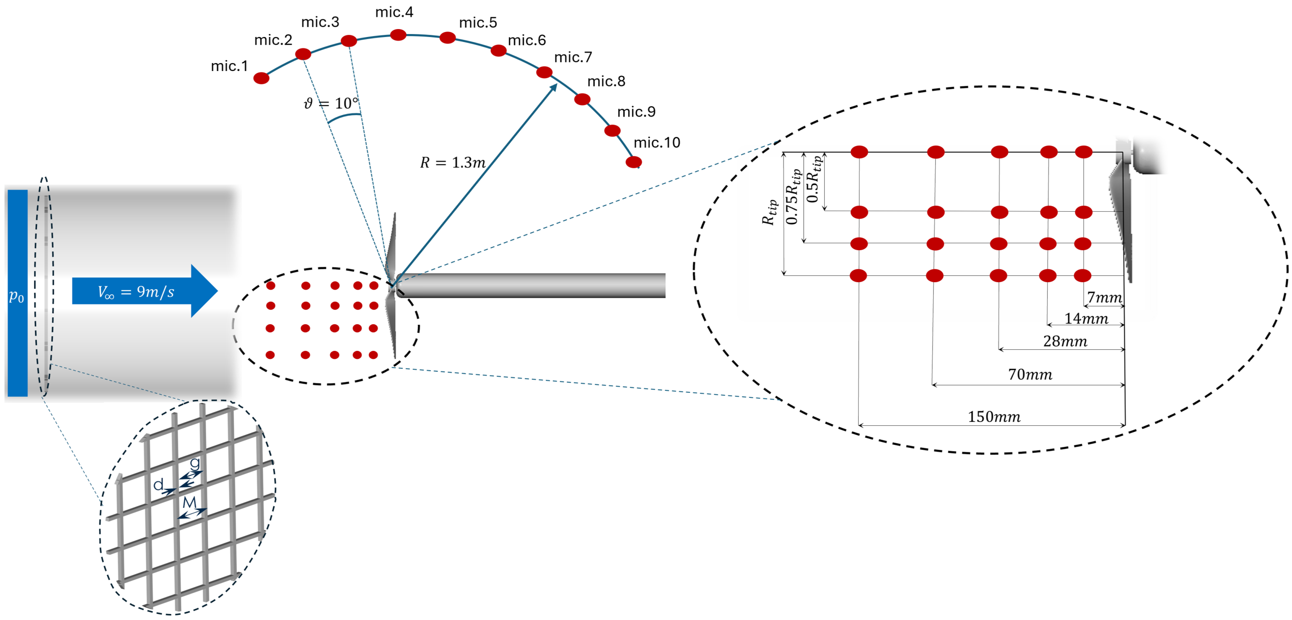

Figure 1: Numerical setup and turbulence grid - $g = 9cm$, $d = 1cm$, $M = 10cm$

is enclosed into the pipe $0.6m$ upstream from the exit and at $1m$ from the propeller plane. The propeller is the same as previous works [2, 5, 15]; the diameter is $0.3m$ and the airfoil profile is the NACA-4412. The rotational speed is $\Omega = 6000RPM$.

The total pressure p_0 is prescribed as a boundary condition upstream of the grid to match the reference mean velocity value $V_\infty = 9m/s$. It is computed accounting for the local pressure losses introduced by the grid, Δp^0 as [16]:

$$\frac{\Delta p^0}{q} = A\Big(\frac{1}{\beta^2} - 1\Big)^B, \tag{1}$$

where q is the upstream dynamic pressure, β is the grid porosity, and A and B are functions of Reynolds number, Mach number, and grid geometry. For a square-mesh grid, porosity is given by:

$$\beta = \Big(1 - \frac{d}{M}\Big)^2 \tag{2}$$

Free-stream and ambient static pressure are imposed as boundary conditions at the borders of the computational domain to prevent flow recirculation.

20 probes are distributed upstream of the propeller plane to characterize the inflow (fig.1). After 3 initial settling revolutions, data are sampled for 10 revolutions with sampling frequency $f_s = 20kHz$. The signal is then divided into 4 Welch blocks with 50% overlap, resulting in a resolution frequency $\Delta f = 20Hz$. Surface pressure is sampled at $f_s = 367kHz$ with a spatial averaging of $0.4mm$ over the propeller and nacelle surfaces to feed the FWH analogy and obtain acoustic spectra.

The setup for the clean case is obtained by removing the turbulence grid and resetting the total pressure. In addition, VR 11, previously used to resolve incoming turbulence, is reduced to an offset of the propeller to keep the same resolution at the propeller while reducing the computational cost.

2.3 Validation

Grid convergence is assessed for all tested cases and the results are validated against data from the reference experiment [12]. Two meshes (coarse and medium) are analyzed. The results of the fine resolution will be presented in the future. The characteristic length M (fig.1) is discretized with 80 and 120 voxels for the coarse and medium grid, respectively.

Since the load cell was not used in the experiment, the numerical thrust and torque coefficients, C_T and C_Q, are compared in tab.1 with the ones available in the literature [2], obtained through a BEMT approach. A good match is observed for all the meshes, with the C_T from the LBM being slightly lower than BEMT prediction.

Table 1: Convergence of C_T and C_Q

	Coarse	Medium	BEMT ([2])
C_T	0.087	0.088	0.09
C_Q	0.008	0.0081	0.008

Table 2 compares the mean velocity V_m, the turbulence intensity TI, and the turbulence integral time scale T_{uu} obtained from the numerical simulations and the experiments at $x/R_{tip} = 1$, $r/R_{tip} = 0.5$ without and with the propeller. The integral time scale T_{uu} is used in the table because the mean velocity gradients introduced by the propeller invalidate Taylor's hypothesis for the computation of the integral length scale $\Lambda_{uu,x}$.

Table 2: Flow quantities at $x/R_{tip} = 1$, $\frac{r}{R_{tip}} = 0.5$

	$V_m[m/s]$		$TI[\%]$		$T_{uu}[s]$	
	Num.	Exp.	Num.	Exp.	Num.	Exp.
wo prop.	9.55	9	6.98	7.13	0.17	0.25
with prop.	10.3	9.68	6.3	6.4	0.16	0.2

Mean velocity and velocity fluctuations are computed considering the velocity measured by the hot wire as described by Zamponi et al. [17].

The integral time scale T_{uu} is obtained as the integral of the autocorrelation function in the interval from its maximum to the point where it decreases to $1/e^2$ [17]. For the case with turbulent inflow, the phase-locked average is subtracted from the instantaneous signal to remove the periodicity introduced by the blade passage. Numerical and experimental results show good agreement, with the numerical V_m being up to $0.6m/s$ higher than the experimental one.

Similarly, the comparison of the turbulence spectra (fig. 2) shows a good agreement on the frequency range considered. The drop in the spectra at the 5^{th} and 8^{th} harmonics of the Blade Passing Frequency (BPF) in the coarse and medium/fine cases, respectively, is due to the filtering effect of the mesh. The numerical scheme requires at least 10 voxels per wavelength to resolve the wave. An increase in the overall resolution will solve the turbulence up to the 10^{th} BPF harmonic, but the computational cost will be prohibitive. However, as proved later, the far-field noise is well captured making the increase of computational cost not needed for the scope of this paper.

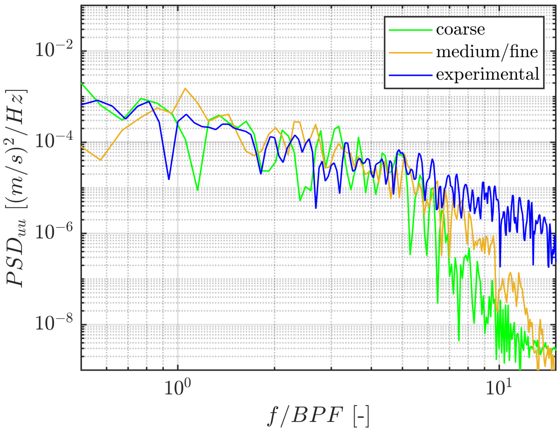

Figure 2: Turbulence spectrum at $x = 1R$, $r/R = 0.5$ without propeller

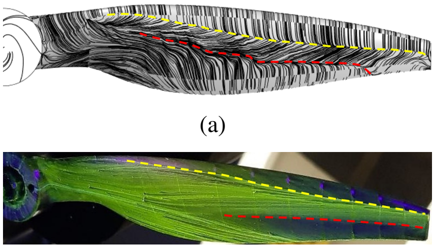

(a)

(b)

Figure 3: Time-averaged surface streamlines 3(a) and oil flow visualization 3(b)

To further support the validation of the numerical database, the time-averaged surface streamlines are compared with oil flow visualization in fig. 3 only for the turbulent case, for conciseness. Separation and reattachment lines, indicated by yellow and red dotted lines, respectively, are slightly delayed with respect to the experimental result. This can be due to the still high y^+, the adopted wall model, and the slightly higher mean velocity in the numerical simulations. Improvement in fine resolution is expected. The effect of different wall models on the LSB prediction will be the objective of future studies.

Acoustic spectrum at mic.1 (fig. 1) is shown for both the turbulent (fig.4(a)) and clean (fig.4(b)) inflows. The slight underprediction (less than $2dB$) at the 1^{st} harmonic, mostly influenced by steady loading and thickness noise, is likely due to the higher numerical mean velocity, which reduces the steady loading, consequently under-predicting C_T. The experimental result at the third harmonic is dominated by motor noise, while the tones at half of the BPF harmonic originate from the motor shaft frequency. For the clean inflow case, the difference between numerical and experimental results from the 3^{th} to the 8^{th} BPF harmonic is likely due to the loaded motor noise, not present in the simulations. The over-prediction at frequencies higher than the 20^{th} harmonic is ascribed to inaccuracies in reattachment point prediction. The mesh refinement from coarse to medium does not affect the acoustics.

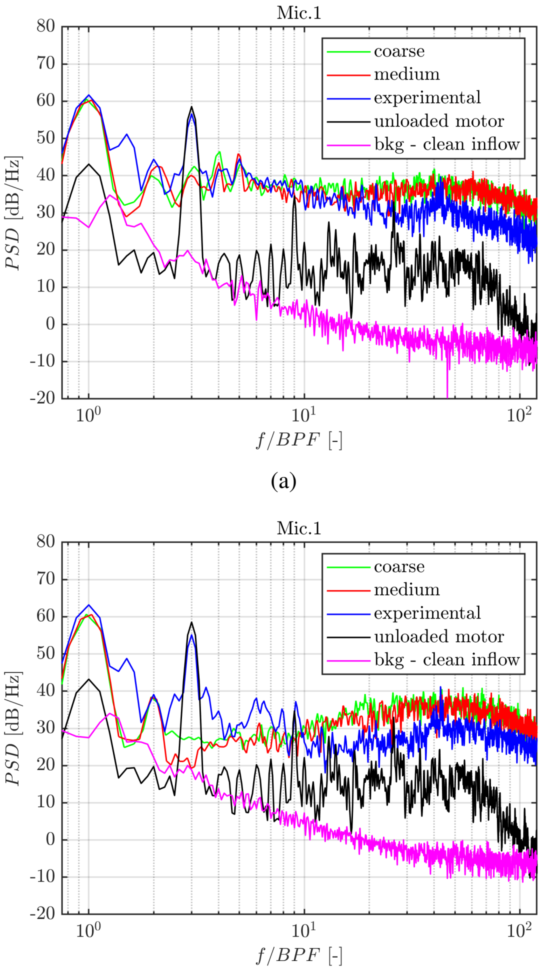

(a)

(b)

Figure 4: (a) Acoustic spectra for turbulent (b) and clean inflow

3. RESULTS AND DISCUSSION

3.1 Characterization of turbulence

3.1.1 Absolute frame of reference

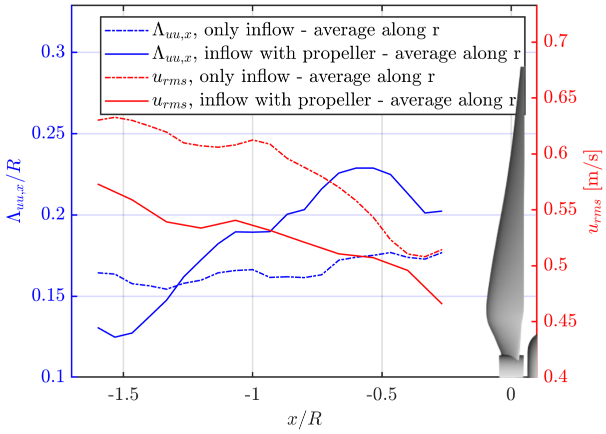

Figure 5: $\Lambda_{uu,x}(x)$ and $u_{rms}(x)$, radially averaged, with and without the propeller

Figure 5 shows the evolution of the integral length scale $\Lambda_{uu,x}(x)$ and root mean square $u_{rms}(x)$, with and without the propeller. The quantities have been radially averaged to highlight the general trend, although inhomogeneity remains present along the span. It can be observed that, without the propeller, $\Lambda_{uu,x}$ is almost constant, with $\Lambda_{uu,x} \approx 2.4cm$. In the presence of the propeller, the integral length scale grows faster approaching the propeller plane, as a result of the stream tube contraction. $u_{rms}(x)$ presents lower values and a faster decay in the presence of the propeller because of the stream tube contraction that, while elongating the eddies in the streamwise direction, reduces the fluctuation of the axial component.

3.1.2 Relative frame of reference

The analysis presented in this section refers to a plane at $r/R_{tip} = 60\%$ in the rotating frame of reference, normal to the spanwise direction (fig. 6(a)). The in-plane components, u, and v are projected along the mean local direction to obtain u_t and v_t, the tangential and normal components, respectively, relative to the mean streamline (fig. 6(b)), while w_t is the out-of-plane component.

Figure 7 presents the root mean square of the three velocity components along the mean stagnation line. Approaching the propeller plane, u_t decelerates and $u_{t,rms}$ decreases, while $v_{t,rms}$ increases, and w_t shows a weaker

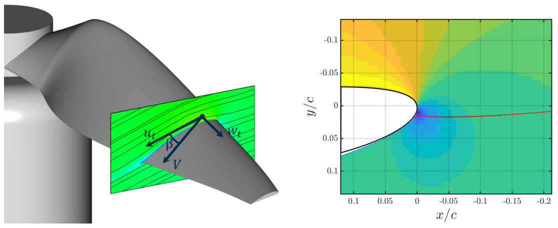

(a) (b)

Figure 6: (a) Visualization of the rotating frame of reference and (b) mean stagnation line s at $r/R = 60\%$

increase. This observation suggests a momentum transfer from u_t to v_t, aligning with the physical description of the Rapid Distortion Theory (RDT) [18] showed with the dashed line in the figures.

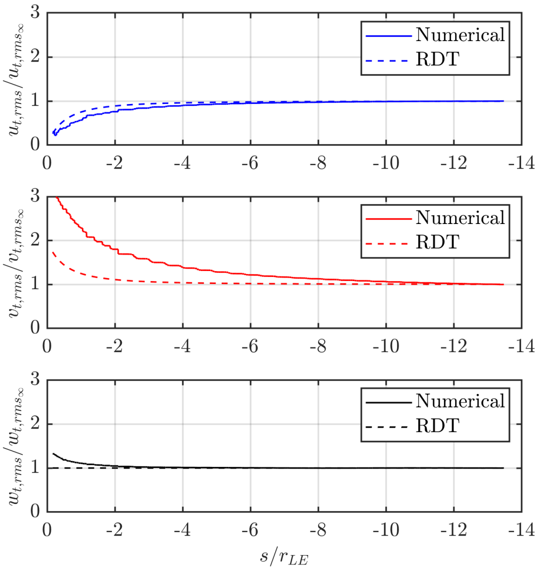

Figure 7: $u'_{t,rms}$, $v'_{t,rms}$ and $w'_{t,rms}$ along the mean stagnation line

More specifically, $u_{t,rms}$ obtained from the numerical simulations follows the RDT prediction well up to $-4r_{LE}$, then approaching the stagnation point it decreases a bit faster than predicted; $v_{t,rms}$ diverges from the RDT prediction already at $s = -10r_{LE}$, reaching values up to 3 times the undisturbed level. The early increase in $v_{t,rms}$, occurring before the decrease in $u_{t,rms}$, suggests the existence of an additional mechanism - beyond the momentum transfer from the streamwise component - that enhances $v_{t,rms}$. In this case, a possible explanation can lie in the curvature of the mean streamline, which is not accounted for in RDT: streamwise velocity fluctuations induce oscillations in the centrifugal force acting on fluid particles, leading to fluctuations in the radial pressure gradient. These fluctuations influence the normal velocity component. To validate this hypothesis, a comparison with a 2D simulation of a wing section will be conducted in future studies.

Figure 8 shows the spatial distribution of the integral length scales $\Lambda_{u_t u_t,s}(s)$ and $\Lambda_{v_t v_t,span}(s)$ along the mean stagnation line. These quantities are normalized with respect to their value at $s/r_{LE} = -6$. Approaching the leading edge, $\Lambda_{u_t u_t,s}(s)$ decreases, while $\Lambda_{v_t v_t,span}(s)$ increases. This indicates that vortices are compressed against the leading edge and elongated in the spanwise direction, enhancing the spanwise coherence of normal velocity fluctuations.

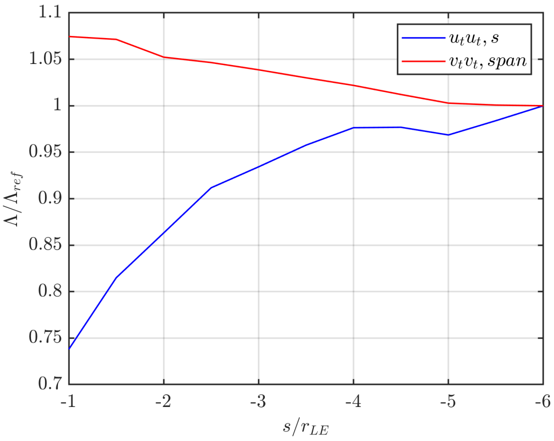

Figure 8: Spatial distribution of the integral length scales $\Lambda_{u_t u_t,s}(s)$ and $\Lambda_{v_t v_t,span}(s)$ along the mean stagnation line

3.2 Laminar separation bubble

The time-averaged surface streamlines, superimposed to the standard deviation of the surface pressure fluctuations coefficient c_{p_σ}, are shown in fig. 9 for both turbulent and clean inflows. No significant difference is observed in the mean flow features of the LSB, visualized through

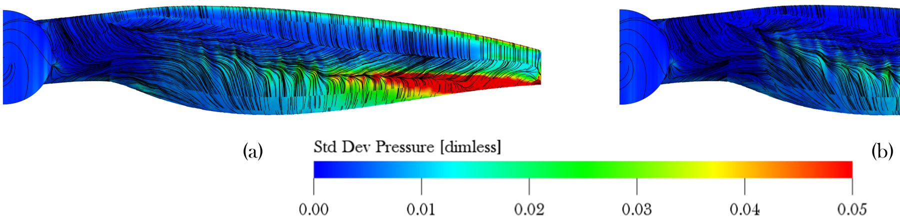

Figure 9: Time-averaged surface streamlines, superimposed to the standard deviation of the surface pressure fluctuations coefficient c_{p_σ} over the blade surface for turbulent (a) and clean (b) inflow

the surface streamlines. The impact of turbulence on noise sources becomes evident by looking at c_{p_σ}. Incoming turbulence increases the amplitude of the surface pressure fluctuations at the leading edge, along the separation line, and inside the bubble itself. This suggests that incoming turbulence enhances the unsteadiness of the LSB.

3.3 Far-field noise

Figure 10 shows the far-field noise spectrum at mic.1 for the turbulent and clean inflows, while the noise sources are described in fig. 11.

Ingested turbulence increases broadband noise up to the 30^{th} harmonic and introduces tones at the harmonics higher than the 2^{nd}. The first harmonic is dominated by the steady loading and therefore is not affected by the presence of free-stream turbulence. At $f > 30BPF$, where trailing-edge noise is the dominant source, all the spectra collapse meaning that the surface pressure fluctuations at the trailing edge are weakly affected by the inflow turbulence .

Figure 11 shows the constructive (CP) and destructive (DP) contribution maps, expressed in dB, to the far-field noise at mic.1 in the frequency $1.3kHz < f < 1.5kHz$, where the difference between the turbulent and clean acoustic spectra is $5dB$. CP and DP are computed from the coherence between the acoustic pressure radiated from the surface element and the total acoustic pressure at the same location ([3]). The CP map shows noise sources, that constructively interfere, due to inflow turbulence at the leading edge and on the suction side up to the laminar separation bubble. The DP map shows that the leading edge, in clean inflow, generates destructive contribution in this frequency range, which is canceled in the turbulent case. After reattachment, the sources are influenced by the mean LSB characteristics and therefore they are not affected by the ingested turbulence.

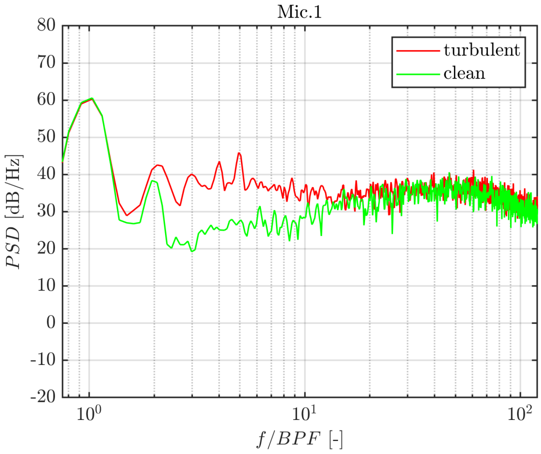

Figure 10: Acoustic spectrum for turbulent and clean inflow at mic.1

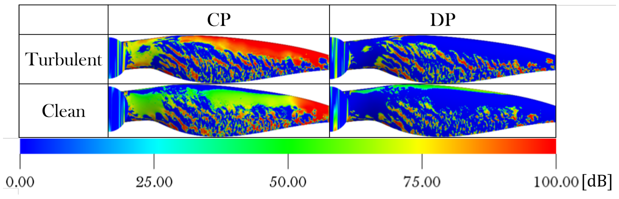

Figure 11: constructive (CP) and destructive (DP) contribution maps for turbulent and clean inflow

4. CONCLUSIONS

This paper investigated the interaction of a low Reynolds propeller with incoming turbulence, both in terms of turbulence distortion and the impact of turbulence on the generated far-field noise. Streamtube contraction induces elongation of the largest eddies in the streamwise direction, reducing the intensity of u_{rms}, while the leading edge distortion increases the intensity and spanwise coherence of normal fluctuations. These results will be exploited in a future work to evaluate the performances of Amiet's model when turbulence distortion is taken into account. In addition, incoming turbulence was shown to have an impact on the unsteady behavior of the laminar separation bubble, increasing the unsteady loading on the blade. In this configuration, trailing edge noise is not affected by ingested turbulence.

5. ACKNOWLEDGMENTS

The authors acknowledge Compagnia di San Paolo for funding and supporting the present project and ISCRA for the providing computational resources.

6. REFERENCES

[1] M. M. Connors, "Factors that influence community's acceptance of noise: An introduction for urban air mobility," tech. rep., 2019.

[2] D. Casalino, G. Romani, R. Zhang, and H. Chen, "Lattice-boltzmann calculations of rotor aeroacoustics in transitional boundary layer regime," *Aerospace Science and Technology*, vol. 130, p. 107953, 2022.

[3] D. Casalino, G. Romani, L. M. Pii, and R. Colombo, "Flow confinement effects on suas rotor noise," *Aerospace Science and Technology*, vol. 143, p. 108756, 2023.

[4] C. S. Thurman, N. S. Zawodny, and N. A. Pettingill, "The effect of boundary layer character on stochastic rotor blade vortex shedding noise," in *The Vertical Flight Society's 78th Annual Forum and Technology Display*, 2022.

[5] E. Grande, G. Romani, D. Ragni, F. Avallone, and D. Casalino, "Aeroacoustic investigation of a propeller operating at low reynolds numbers," *AIAA Journal*, vol. 60, no. 2, pp. 860–871, 2022.

[6] E. Grande, D. Ragni, F. Avallone, and D. Casalino, "Laminar separation bubble noise on a propeller operating at low reynolds numbers," *AIAA Journal*, vol. 60, no. 9, pp. 5324–5335, 2022.

[7] M. Sevik, "Sound radiation from a subsonic rotor subjected to turbulence," *Fluid Mech., Acoustics, and Design of Turbomachinery, Pt. 2*, 1974.

[8] W. K. Blake, "Mechanics of flow-induced sound and vibration. volume 1 general concepts and elementary source. volume 2-complex flow-structure interactions," *Aplikace Matematiky, Applied Mathematics*, vol. 1, 1986.

[9] D. B. Hanson, "Spectrum of rotor noise caused by atmospheric turbulence," *The Journal of the Acoustical Society of America*, vol. 56, no. 1, pp. 110–126, 1974.

[10] R. K. Amiet, "Acoustic radiation from an airfoil in a turbulent stream," *Journal of Sound and vibration*, vol. 41, no. 4, pp. 407–420, 1975.

[11] R. Amiet, "Noise produced by turbulent flow into a propeller or helicopter rotor," *AIAA Journal*, vol. 15, no. 3, pp. 307–308, 1977.

[12] G. Capobianchi, S. Montagner, A. Piccolo, A. Di Marco, F. Avallone, G. Cafiero, D. Ragni, E. de Paola, and L. G. Stoica, "Impact of turbulent inflow on the far-field noise generated by a propeller operating at low reynolds number," in *30th AIAA/CEAS Aeroacoustics Conference (2024)*, p. 3154, 2024.

[13] J. Christophe, J. Anthoine, and S. Moreau, "Amiet's theory in spanwise-varying flow conditions," *AIAA journal*, vol. 47, no. 3, pp. 788–790, 2009.

[14] H. Raposo and M. Azarpeyvand, "Turbulence ingestion noise generation in rotating blades," *Journal of Fluid Mechanics*, vol. 980, p. A53, 2024.

[15] L. van Beek, "The distortion of turbulence by a low reynolds number uav propeller and the effect on aeroacoustics: An analytical and experimental study," 2021.

[16] P. Roach, "The generation of nearly isotropic turbulence by means of grids," *International Journal of Heat and Fluid Flow*, vol. 8, no. 2, pp. 82–92, 1987.

[17] R. Zamponi, S. Satcunanathan, S. Moreau, D. Ragni, M. Meinke, W. Schröder, and C. Schram, "On the role of turbulence distortion on leading-edge noise reduction by means of porosity," *Journal of Sound and Vibration*, vol. 485, p. 115561, 2020.

[18] J. Hunt, "A theory of turbulent flow round two-dimensional bluff bodies," *Journal of Fluid Mechanics*, vol. 61, no. 4, pp. 625–706, 1973.